Indian Journal of Advances in Chemical Science

Article

Photocatalytic Oxidation Using Cobalt Oxide Nanoparticles for Dye Removal

S. Vijayalakshmi[1], I. Sharmila Lydia[1], D. Vasudevan[2]*

[1]Department of Chemistry, Bishop Heber College, Tiruchirappalli, Tamil Nadu, India, [2]Division of Electrodics and Electrocatalysis, Central Electrochemical Research Institute, Karaikudi, Tamil Nadu, India

ABSTRACT

In recent years, photocatalytic oxidation using semiconductor nanoparticles (NPs) has gained global attention as a method for wastewater treatment. In view of this, the present work reports the results of the investigations on the use of cobalt oxide (CoO) NPs on the photocatalytic degradation of methyl violet (MV). The CoO NPs were synthesized by a hydrothermal route and were then characterized using Fourier-transform infrared, ultraviolet diffuse reflectance spectroscopy, ultraviolet–visible, Raman, X-ray diffraction, vibrating-sample magnetometer, transmission electron microscopy, scanning electron microscope, and Energy dispersive X-ray spectroscopy (EDAX) techniques. The NPs were found to be spherical and in size range of 3–5 nm. The NPs were also subject to calcination in the temperature range of 150–350°C. The temperature of calcination seemed to influence the surface composition of CoO. Both calcined and uncalcined CoO NPs were then subject to studies on the degradation of MV. The CoO 350 NPs exhibited the best photocatalytic degradation efficiency of 73% for the degradation of MV.

Key words: Photocatalytic oxidation, Cobalt oxide nanoparticles, Dye degradation.

1. INTRODUCTION

The textile industry generates large amount of industrial effluents and is a major source of water pollution which is not only harmful for aquatic life but also mutagenic to human. Textile wastewater includes a large variety of dyes and chemical additions that make the environmental challenge [1-3] for textile industry not only as liquid waste but also in its chemical composition. Main pollution in textile wastewater comes from dyeing and finishing processes. These processes require the input of a wide range of chemicals and dyestuffs. Water is used as the principal medium to apply dyes and various chemicals for finishes. Because all of them are not contained in the final product, they become waste and caused disposal problems. Major pollutants in textile wastewaters are high suspended solids, chemical oxygen demand (COD), heat, color, acidity, and other soluble substances. Substances that need to be removed from textile wastewater are mainly COD, biochemical oxygen demand, nitrogen, heavy metals, and dyestuffs.

There are more than 10,000 dyes used in textile manufacturing alone nearly 70% being azo dyes. A major source of color release into the environment is associated with the incomplete exhaustion of dyes onto the textile fiber from an aqueous dyeing process and the need to reduce the amount of residual dye in the textile effluent has become a major concern in recent years. Azo dyes have -N=N- as the chromophore and are highly carcinogenic to flora and fauna and are not easily degradable [4].

The environmental threats posed by these chemicals could be solved by the use of high-performance visible light active photocatalysts [5-7]. As an ultimate solution for clean water, the synthesis of photocatalyst which could harvest sunlight has been regarded as the "holy grail" in material synthesis [8,9]. Recently, metal oxide semiconductors seem to find wide spread applications in the fields, including optics, electronics, catalysis, sensors, magnetic materials, and so on due to their large surface to volume ratio, high charge separation, morphology, size, and structure.

Various metal oxide semiconductor materials including TiO_2 [10-12], ZnO [13-16], CdS [17,18], ZnSe, WO_3 [19,20], Ga_2O [21], Fe_2O_3, and Fe_3O_4 have been thoroughly studied for photo catalysis and water splitting. Furthermore, MoO materials with specific properties suitable for photocatalytic applications could be prepared by controlling the synthetic strategies [22,23].

Among the metal oxides, cobalt oxide (CoO) is a novel, environment-friendly, magnetic, single component, highly abundant low-cost photocatalyst with a narrow band gap (2.4 eV) for the absorption of visible light and with very high solar to hydrogen efficiency [24]. It is a p-type semiconductor with interesting magnetic and electronic properties which are essential for photodegradation of organic contaminants in water bodies [25]. Further, CoO has its absorption edge in the visible region, which also proves its potential application in photocatalysis [26]. Cobalt monoxide exists in two phases: Stable rock salt phase and less stable Wurtzite phase in which Co (II) is tetrahedral and octahedral coordinated. The face-centered cubic (fcc) CoO holds a thermodynamically stable state, but the hexagonal close-packed structure is relatively unstable and can be converted into a cubic structure by the application of heat and pressure [27-31]. The fcc CoO also can be oxidized to spinel Co_3O_4 at a suitable temperature and also the spinel Co_3O_4 can be easily reconverted to CoO by annealing under high vacuum [32]. The CoO nanoparticles (NPs) with <10 nm size have been reported to be effective in water splitting.

***Corresponding author:**

E-mail: vasudevand2016@gmail.com

ISSN NO: 2320-0898 (p); 2320-0928 (e)

DOI: 10.22607/IJACS.2019.704004

Received: 05th November 2019;
Revised: 30th November 2019;
Accepted: 03th December 2019

Special requirements are necessary to keep cobalt in a low valence state. The CoO NPs have less stability and become deactivated after an hour of reaction due to their aggregation. Furthermore, the CoO NPs are too small to be recycled. This may shoot up their costs. For practical applications, it is highly imperative to improve their stability and lower the cost. This is a challenge and so only very few studies have focused on their synthesis [33].

Yin and Wang have synthesized 5 nm sized tetrahedral CoO nanocrystals through the oxidation of $Co_2(CO)_8$ in toluene in the presence of sodium bis(2-ethylhexyl) sulfosuccinate [N(AOT)] at 130°C. By the decomposition of Co (II) Cupferronate in decalin, pure CoO NPs in the size range of 4.5–18 nm were synthesized through solvothermal route [28c]. Jana *et al.* have prepared Co_3O_4 nanocrystals by the pyrolysis of cobalt carboxylate salts in a hydrocarbon solvent. An *et al*. have reported the synthesis of pencil-shaped CoO by thermal decomposition of cobalt oleate complex [29c].

The present work reports the fabrication of CoO nanoflowers as photocatalyst for the degradation of methyl violet (MV). Due to the complicated aromatic moiety, azo dyes are thermally stable and thus difficult to be degraded.

The CoO nanoflowers were prepared through a facile two-step process – first, the formation of cobaltous hydroxide through a hydrothermal method and second, the transformation to CoO nanoflowers by an annealing process. Different annealing temperatures significantly alter the morphologies, structure, and size of the CoO nanoflowers.

2. EXPERIMENTAL SECTION

2.1. Materials

Cobaltous chloride (98%), ammonium hydroxide (97%), and ethanol were purchased from Aldrich and used as received. MV (Analytical Reagent grade) was purchased from Eastman Company and was used as such. Double distilled water was used in all the experiments.

2.2. Preparation of CoO NPs

In a typical hydrothermal synthesis, 2.7 g of cobaltous chloride ($CoCl_2.6H_2O$) was dissolved in 100 ml water followed by the addition of 30 ml ethanol under vigorous stirring at 45°C for 0.5 h. Ammonia was then added dropwise (0.2 M, 2.5 ml) to the clear solution under stirring at 80°C. The precipitation of CoO takes place slowly. The final suspension was transferred into a 100 ml Teflon-lined autoclave and maintained at 150°C for 3 h. After cooling to room temperature, the CoO precipitate was centrifuged and washed with acetone thrice and then dried at 60°C for 6 h [7-10,34-37]. The as-synthesized CoO NPs were subjected to an annealing process at temperatures 150, 250, and 350°C for 3 h with a constant heating rate of ±2°C min^{-1} and the samples labeled as CoO 150, CoO 250, and CoO 350 accordingly.

2.3. Characterization

The crystallite structures of the as-synthesized samples were characterized by powder X-ray diffraction (XRD) using Philips X' pert Pro X-ray diffractometer using Cu Kα radiation with a scan rate of 2θ/min^{-1} in the range of 10–80°. Infrared (IR) spectra of the KBr pellets of CoO NPs were recorded with a PerkinElmer 4000 cm^{-1}–400 cm^{-1} Fourier-transform-IR (FT-IR) spectrophotometer. The ultraviolet–visible (UV–vis) absorption spectra were recorded out on PerkinElmer Lambda 35 Spectrophotometer from 190 nm to 1100 nm with 1 cm path length. The microstructures and morphologies of the samples were observed by a scanning electron microscopy (SEM) measurements were performed on ZEISS JEOL JSM-T220A operating at 10–3 kV in high vacuum. UV–vis diffuse reflectance spectra (DRS) were conducted on a Cary 100 UV–vis spectrophotometer, and $BaSO_4$ was used as a reflectance standard. Raman STR 500 mm focal length laser Raman Spectrometer was employed for Raman spectral studies.

2.4. Photocatalytic Studies

The photocatalytic activity of the as-synthesized CoO NPs was evaluated by the degradation of MV in aqueous solution under direct sunlight irradiation. Around 20–40 mg of catalyst was added into a 50 ml dye solution (2×10^{-5} M). The suspension containing the dye and the catalyst was stirred for 15–20 min in the dark to reach adsorption-desorption equilibrium of the dye on the surface of the material. Then, the suspension was exposed to direct solar light irradiation with constant stirring at specified time intervals. About 3 ml of the solution was taken, centrifuged to remove the catalysts (2500 rpm, 5 min) and the supernatant clear solution was analyzed using a UV–vis spectrophotometer (absorbance at λmax=580 nm for the dye). An aquarium air pump was used to provide an unstinted air supply. The percent degradation (%D) was calculated using the relation $\%D = \frac{A_0 - A_t}{A_0} \times 100$; where A_0=Initial concentration of MV before irradiation and At is the concentration of MV at illumination time "t" [5,6,21,22].

3. RESULTS AND DISCUSSION

3.1. Characterization

The powder XRD patterns of the CoO annealed at different temperatures are displayed in Figure 1. From the figure, the positions and relative intensities of the five characteristic peaks could be indexed with the standard pattern of the typical fcc with lattice constants of a=2.4300 Å, b=1.2429 Å, and c=1.5418 Å [13,20,23]. These diffraction peaks seen at 36.2°, 42.3°, 61.9°, 74.0°, and 78.0°, respectively, are of cubic phase which corresponds to (111), (200), (220), (311), and (222) planes and match well with the JCPDS file No. 78-0431. The crystalline nature CoO is evident due to strong and sharp diffraction peaks. The sample was phase pure. The CoO NPs, even after being calcined at different temperatures (150°, 250°, and 350°C), still retain the fcc phase. However, the intensity of these peaks was slightly altered, which might be due to the discrepancy in the degree of crystallinity. The diffraction peaks recorded for CoO 350 were much narrower than those observed for the other samples, indicating that CoO 350 has higher crystallinity. When the calcination temperature was increased above 350°C, the crystalline nature was reduced.

3.2. SEM Analysis

The SEM images of the CoO NPs annealed at different temperatures are displayed in Figure 2. The CoO NPs appear to be spherical. After annealing, the prepared CoO samples are a collection of small NPs, with the porous structure and spherical shape. The flake-like morphology of the CoO NPs is well maintained at the calcination temperature of 350°C while the NPs on the surface become larger with an increase in annealing temperature at 350°C.

3.3. EDAX Analysis

The EDAX images of CoO 350 and CoO are shown in Figure 3. The atomic % of Co and O is found to be 52 and 47, respectively.

3.4. FTIR

The FTIR spectra of as-synthesized CoO NPs are presented in Figure 4. The Co-O stretch appears as a sharp peak at 420 cm^{-1}. The

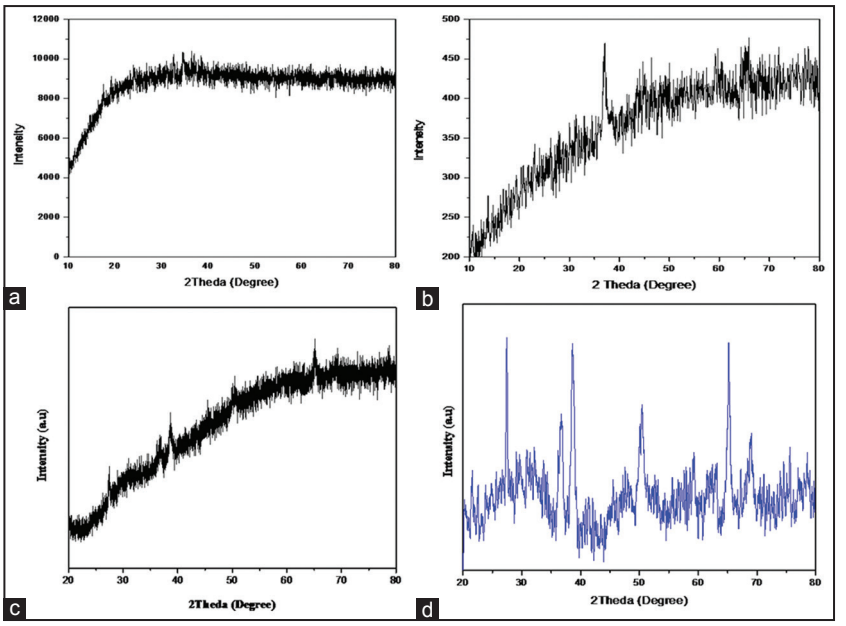

Figure 1: Powder X-ray diffraction patterns of as-synthesized cobalt oxide nanoparticles at different annealing temperatures (a) CoO NA, (b) CoO 150, (c) CoO 250, (d) CoO 350.

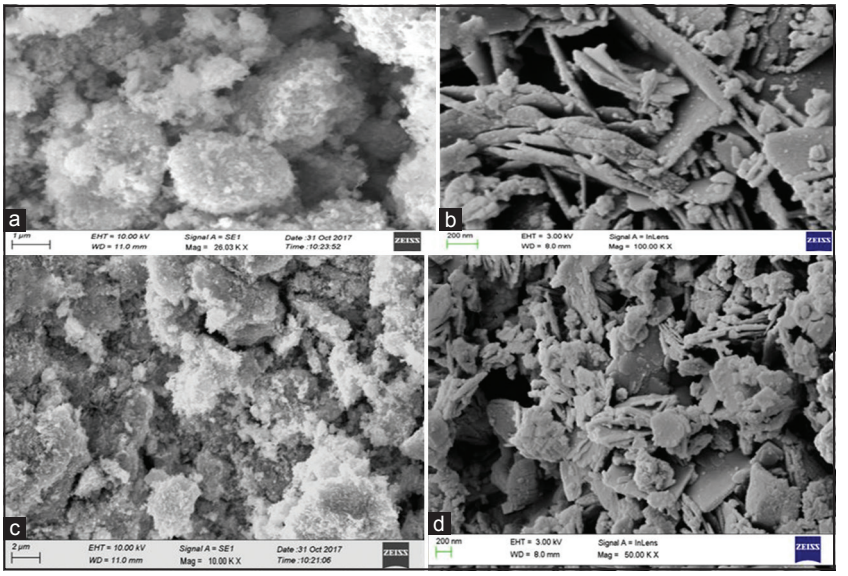

Figure 2: Scanning electron microscope images as prepared and annealed samples of cobalt oxide (CoO), (a) CoO, (b) CoO 150, (c) CoO 250, (d) CoO 350.

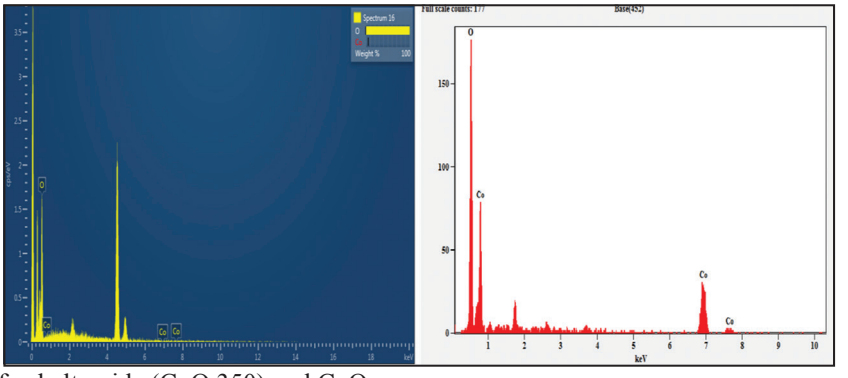

Figure 3: EDAX image of cobalt oxide (CoO 350) and CoO.

broadband at around 3450 cm^{-1} is due to -OH stretching deformation. The presence of -OH group could be due to the adsorbed water. The characteristic peaks observed in the IR spectrum are also found to be in good agreement with the fcc structure of CoO [33].

3.5. UV–vis Spectra

The UV–vis absorption spectrum of CoO NPs calcined at different temperatures is shown in Figure 5. The size-dependent features of the CoO NPs could be confirmed from these results. The absorption bands positioned around 385 and 750 nm correspond to O^{2-} Co^{2+}.

Due to quantum confinement, the nanostructures possess larger band gaps than the corresponding bulk materials. Due to this, the absolute potentials of conduction and valance band edges have to be adjusted.

To differentiate the catalytic activity between the nanostructure and the bulk material and also to investigate the quantum size effect on the catalytic activity of CoO NPs, their band gaps were measured using UV-DRS. Figure 6 shows the UV-DRS spectra of both the samples. The corresponding band gaps (eV) were calculated from the modified Kubelka-Munk function, and the corresponding plots are shown in Figure 7.

The reflectance spectra show a strong absorption in the visible region of 400–800 nm. This suggests that the as-synthesized sample exhibits a stronger visible light absorption indicating enhancement of visible light harvesting.

The photocatalytic activity is controlled by two key factors: The light absorption capability of the materials and the position of conduction used. To determine the light absorption capacity of CoO NPs annealed at different temperatures, UV–vis DRS spectra of each sample were measured.

As shown in Figure 7, all three samples show similar absorption range and the band gaps of the three calcined samples are almost similar and close to 2.6 eV.

The band gaps (Eg) of CoO NPs annealed at various temperatures can be obtained according to the formula $(\alpha h\nu)=(C\ h\nu-Eg)^{n/2}$ where α, ν, h, and C are the absorption coefficient, the incident light frequency, Planck's constant, and a constant, respectively. The variable "n" depends on the characteristics of the optical transition of the semiconductor. For direct semiconductors, "n" equals four and for indirect semiconductors "n" equals one [38]. Thus, the band gap energy of the as-synthesized CoO NPs was estimated from a plot of $\alpha h\nu^2$ versus hν. The intercept of the tangent in the X-axis approximately equals the Eg values of the CoO NPs. The calculated Eg values are 1.5 eV (CoO 150), 1.5 eV (CoO 250), and 1.5 eV (CoO 350). It confirms that the CoO 350 sample has a slightly lower band gap than the other samples of CoO which is in good agreement with their lower reflectance value. The other absorption of band gap energy around 2 eV may be due to the transition of electrons from the "d" band of Co^{2+} to the conduction band (CB) of CoO [39].

The lower band gap of CoO 350 compared to other samples indicates higher solar energy harvesting ability, which in turn is responsible for the production of e^-–h+ pairs resulting in higher photocatalytic activity.

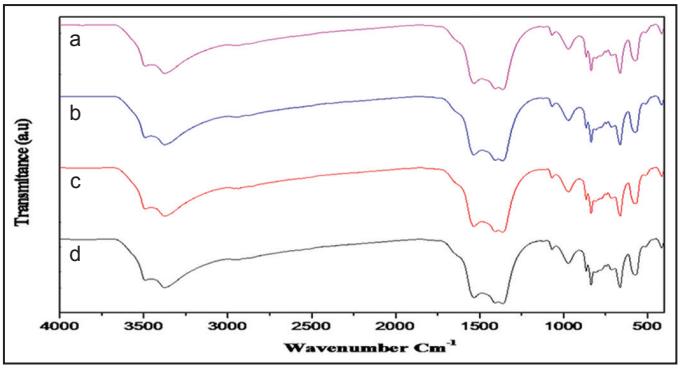

Figure 4: Fourier-transform infrared spectra of (a) cobalt oxide (CoO), (b) CoO 150, (c) CoO 250, (CoO 350).

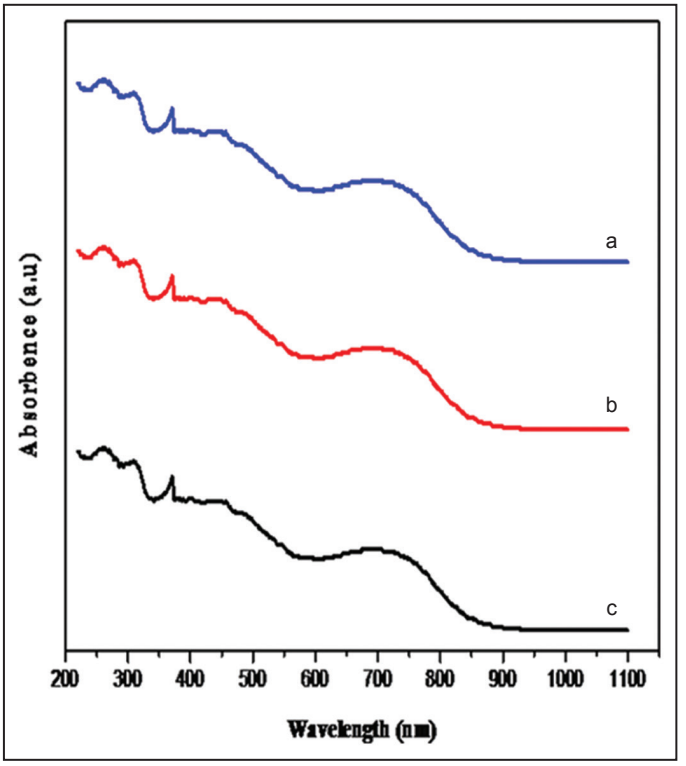

Figure 5: Ultraviolet–visible spectra for (a) cobalt oxide (CoO 150), (b) CoO 250, (c) CoO 350.

3.6. Transmission Electron Microscopy (TEM) Analysis

The field-emission TEM images of the CoO NPs are shown in Figure 8. The CoO 350 NPs appear as needle-shaped. The fcc CoO NPs imaged

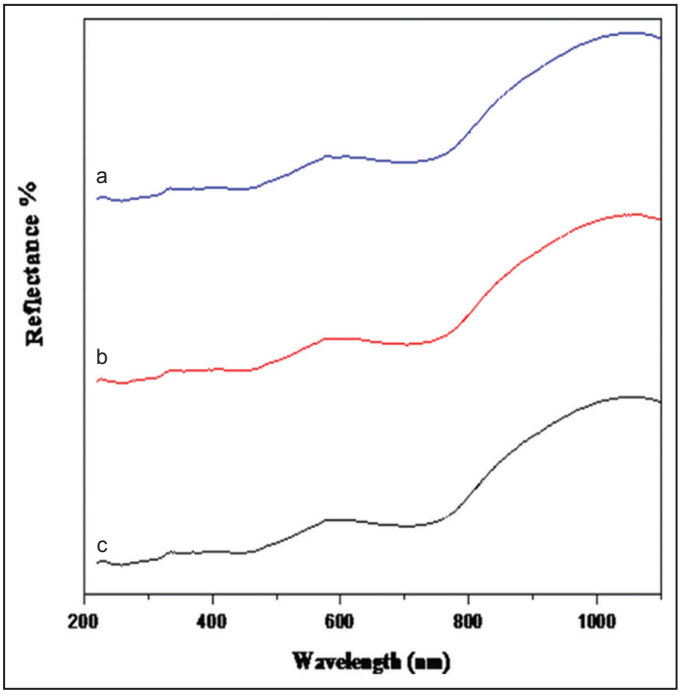

Figure 6: Ultraviolet diffuse reflectance spectra of (a) cobalt oxide (CoO 150), (b) CoO 250, (c) CoO 350.

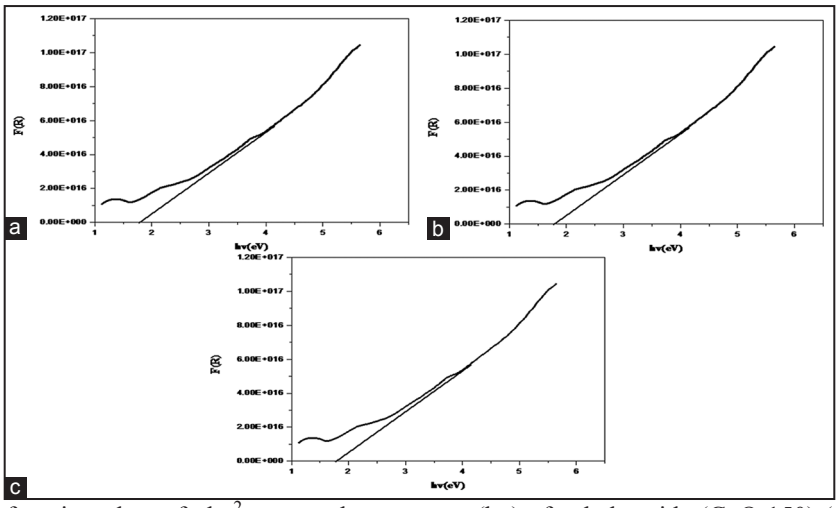

Figure 7: Kubelka-Munk function plots of $\alpha h\upsilon^2$ versus photo energy ($h\upsilon$) of cobalt oxide (CoO 150) (a), CoO 250 (b), and CoO 350 (c).

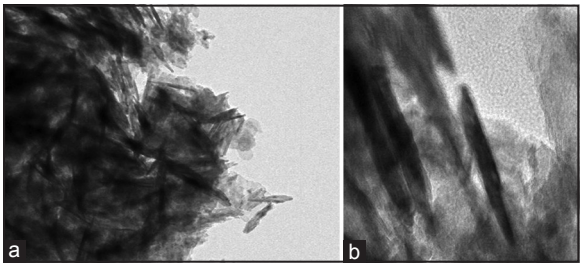

Figure 8: Field-emission transmission electron microscopy images of (a) cobalt oxide (CoO), (b) CoO 350 nanocrystals.

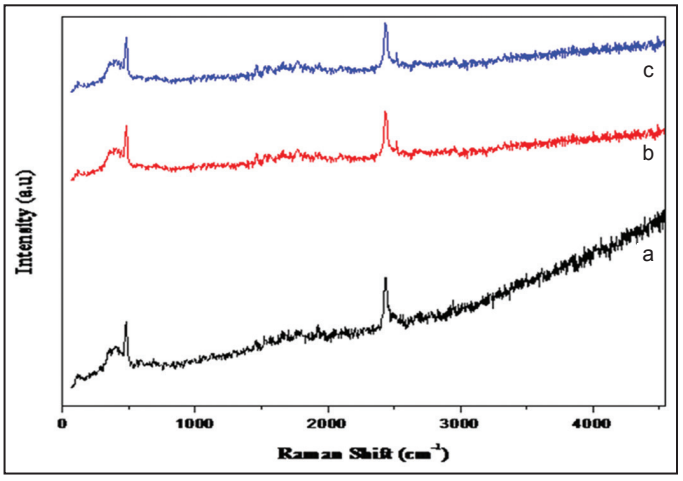

Figure 9: Raman spectra of (a) cobalt oxide (CoO) 150, (b) CoO 250, and (c) CoO 350.

along (001) and (111) zone [40]. The size of the CoO 350 NPs was in the range of 15–20 nm.

3.7. Raman Spectral Studies

The Raman spectra of the nanocrystals of CoO 150, CoO 250, and CoO 350 NPs are shown in Figure 9. The Co^{2+} ions are octahedral coordinated. At least three Raman active modes (A1g, Eg, and T2g) are seen at room temperature [40]. Hence, the Raman spectra of non-calcined and calcined samples were recorded with the lowest possible laser excitation intensity. The particle size of all CoO NPs calculated from the Id/IG value showed the size around 1.9 nm in agreement with the XRD results.

3.8. Photocatalytic Activity of CoO NPs

The photocatalytic activities of the as-synthesized CoO samples calcined at different temperatures were tested by the degradation of the azo dye, MV in aqueous solution under direct sunlight irradiation.

Figure 10a-d shows the UV–vis absorption spectra of (2×10^{-5} M) MV aqueous solution with different photocatalysts, namely, CoO, CoO 150, CoO 250, and CoO 350 followed by the irradiation with direct sunlight for 2 h. The characteristic absorption band of MV dye at 583 nm is monitored as a function of sunlight exposure time. It is evident from Figure 10a-d that annealed samples show higher photocatalytic efficiency compared to the non-annealed CoO sample.

After 120 min of irradiation, the percentage of degradation of MV is only 30% for non- annealed CoO samples (Figure 11). However, the degradation percentage reached up to 35, 47, and 73% using the samples annealed at 150°, 250°, and 350°C, respectively. The sample annealed at 350° C exhibits higher photocatalytic activity. This indicates that the annealing process could enhance the photocatalytic activity of CoO NPs.

The reason may be due to the better crystallinity and lower band gap due to the calcination process. The disappearance of the violet color of MV almost completely with the exposure time of 120 min using CoO 350 samples clearly favors its photocatalytic degradation.

To investigate the photodegradation kinetics Langmuir-Hinshelwood model was used

$$\ln\frac{Co}{Ct}=kt \qquad (1)$$

where "k" is the reaction rate constant and Co is the concentration of MV after adsorption-desorption equilibrium and Ct is the concentration of MV at time "t."

The plot of ln (Co/Ct) versus irradiation time (t) is shown in Figure 12. The straight lines seen in all the plots of ln (Co/Ct) versus t, confirms that the degradation of MV follows pseudo-first-order kinetics. The regression coefficient R^2 is around 0.998±0.001. The rate constants "k" are found to be 0.9837 (CoO), 0.9848 (CoO 150), 0.9897 (CoO 250), and 0.9968 (CoO 350). The result proves that CoO 350 exhibited a higher rate constant for MV degradation, and it is 2^2 times

Table 1: Average particle size, band gap energy, adsorption in dark, and percentage degradation of calcined and non-calcined CoO samples.

Photocatalyst	Average particle size from XRD	UV DRS band gap energy (eV)	Adsorption in dark	% Degradation
CoO	2.1	1.9	2.0	30
CoO 150	2.2	1.8	2.2	35
CoO 250	3.2	1.8	2.6	47
CoO 350	3.3	1.7	3.0	73

CoO: Cobalt oxide, XRD: X-ray diffraction, UV-DRS: Ultraviolet diffuse reflectance spectroscopy

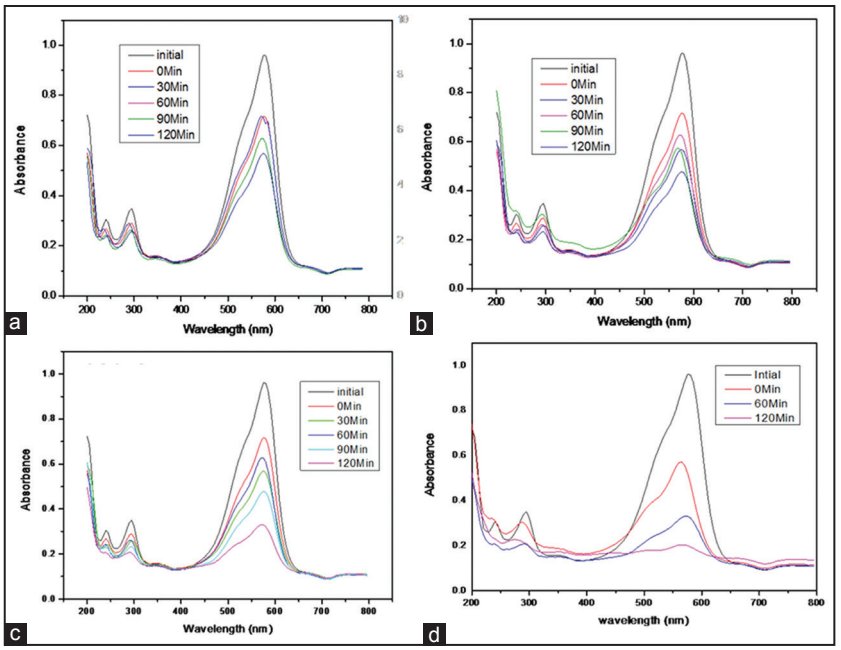

Figure 10: Ultraviolet–visible spectral changes depicting the temporal evolution of the degradation of methyl violet on sunlight irradiation using cobalt oxide (CoO), CoO 150, CoO 250, and CoO 350 for 120 min.

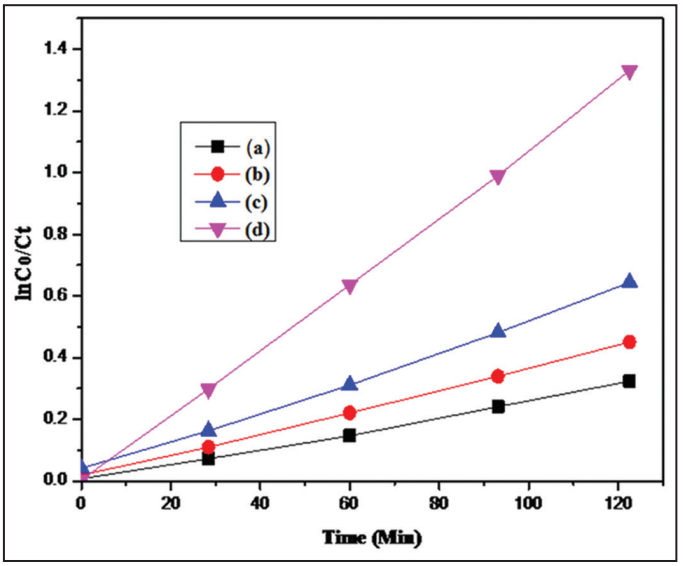

Figure 11: The percentage of dye degradation using cobalt oxide (CoO), CoO 150, CoO 250, and CoO 350 on sunlight irradiation for 120 min. (Dye)=1×10^{-5} M. Catalyst dosage=20 mg/50 ml.

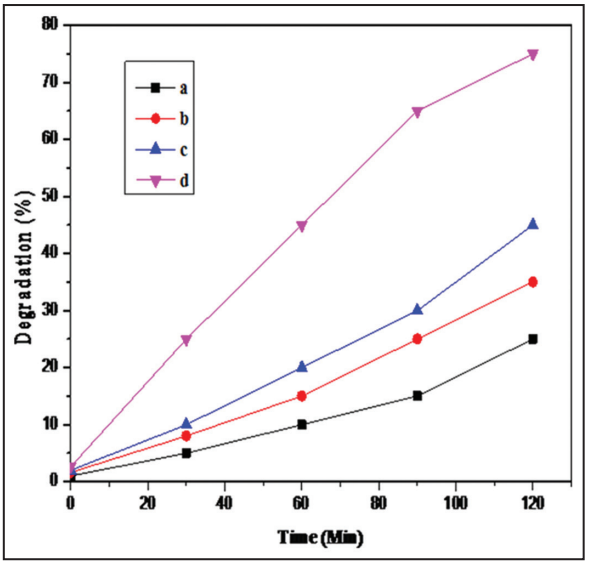

Figure 12: Langmuir-Hinshelwood kinetic plot for the degradation of methyl violet using the as-synthesized cobalt oxide samples.

higher than that for the non-annealed of CoO sample under sunlight irradiation.

The average particle size, band gap energy, adsorption in dark, and the percentage of degradation of various synthesized samples are listed in

Table 1. From the results, it is seen that CoO 350 has a lower Eg value than other samples, suggesting that more light energy can be harvested to excite electrons and holes thereby enhancing the photocatalytic degradation. Therefore, the greater photocatalytic activity of CoO 350 may be attributed to the good crystallinity, lower band gap energy, and lesser average particle size.

3.9. Mechanism of Enhancement of Photocatalytic Activity

During the photocatalytic process, the absorption of photons by CoO leads to the promotion of an electron from the valence band (VB) to CB, thus producing e^{-}–h^{+} pairs. The electron in the CB is removed by the reaction with O_2 in water and the hole in VB can react with hydroxyl ions which are adsorbed on the surface of CoO to produce hydroxyl radical. This hydroxyl (OH.) radical initiates other oxidation reactions. The reactions taking place during the oxidation process of CoO are summarized in Eqs. 2-7.

$$CoO+h\upsilon \rightarrow h^{+}VB+e^{-}_{CB} \quad (2)$$

$$e^{-}_{CB}+O_2 \rightarrow O^{-}_{2} \quad (3)$$

$$O^{-}_{2}+2H^{+} \rightarrow e^{-}_{CB}+H_2O_2 \quad (4)$$

$$H_2O_2 \rightarrow 2OH \quad (5)$$

$$h^{+}_{VB}+H_2O \rightarrow H^{+}+OH \quad (6)$$

$$OHg+dye \rightarrow degradation+pdts \quad (7)$$

4. CONCLUSION

The CoO photocatalysts in the present work were prepared through a hydrothermal method. The structural and optical properties of the resultant materials were characterized by EDAX, SEM, XRD, FTIR, UV–Vis, and UV-DRS spectroscopic techniques. The synthesized materials were highly crystalline. The CoO NPs modification was effective in the temperature range of 150–350°C and results in the reduction of the crystallite size of the NPs. Photocatalytic activity of all samples was determined by analyzing the degradation of MV in the presence of sunlight. CoO 350 caused the material to show significant improvement in the photocatalytic activity. It shows 4 times higher rate of degradation of dye than that by non-calcined CoO. The mechanism of photocatalytic activity was studied by analyzing the emission properties and it was found that the presence of CoO facilitates the interfacial charge–transfer processes in such a way as to utilize the CB electron for enhancing the photocatalytic activity. This trapping of electrons in these materials and as such these material applications could be extended to the developmental purification and energy production processes.

5. CONFLICTS OF INTEREST

The authors declare that they have no conflicts of interest.

6. REFERENCES

1. S. Erdemoğlu, S. K. Aksu, F. Sayılkan, B. Izgi, M. Asilturk, H. Sayılkan, F. Frimmel, S. Guçer, (2008) Photocatalytic degradation of Congo red by hydrothermally synthesized nano crystalline TiO_2 and identification of degradation products by LC–MS, ***Journal of Hazardous Materials,*** **155:** 469-476.
2. J. Wang, Y. Jiang, Z. Zhang, G. Zhao, G. Zhang, T. Ma, W. Sun, (2007) Investigation on the sono catalytic degradation of Congo red catalyzed by nanometer rutile TiO_2 powder and various influencing factors, ***Desalination,*** **216:** 196-208.
3. K. Melghit, M. S. Al-Rubaei and I. Al-Amri, (2006) Photo degradation enhancement of Congo red aqueous solution using a mixture of $SnO_2{\cdot}xH_2O$ gel/ZnO powder, ***Journal of Photochemistry and Photobiology A: Chemistry,*** **181:** 137-141.
4. H. Lachheb, E. Puzenat, A. Houas, M. Ksibi, E. Elaloui, C. Guillard, J. M. Herrmann, (2002) Photocatalytic degradation of various types of dyes (Alizarin S, Crocein Orange G, Methyl Red, Congo Red, Methylene Blue) in water by UV-irradiated titania, ***Applied Catalysis B: Environmental,*** **39:** 75-90.
5. R. M. Navarro, M. C. Sanchez-Sanchez, M. C. Alvarez-Galvan, F. del Valle, and J. L. G. Fierro, (2009) Hydrogen Production from renewable sources: Biomass and photocatalytic opportunities, ***Energy and Environmental Science,*** **2:** 35-54.
6. E. Serrano, G. Rus, J. Garcia-Martinez, (2009) Nanotechnology for sustainable energy, ***Renewable and Sustainable Energy Reviews***, 13: 2373-2384.
7. Y. Tachibana, L. Vayssieres, J. R. Durrant, (2012) Artificial photosynthesis for solar water- splitting, ***Nature Photonics,*** **6:** 511-518.
8. V. A. Sakkas, M. A. Islam, C. Stalikas, T. A. Albanis, (2010) Photocatalytic degradation using design of experiments: A review and example of the Congo red degradation, ***Journal of Hazardous Materials,*** **175:** 33-44.
9. M. Dakiky, I. Nemcova, (2000) Aggregation of o, o'-dihydroxy azo dyes III. Effect of cationic, anionic and non-ionic surfactants on the electronic spectra of 2-hydroxy-5-nitrophenylazo-4-[3-methyl-1-(4"-sulfophenyl)-5-pyrazolone], ***Dyes and Pigments,*** **44:** 181-193.
10. S. Balasubramanian, P. Wang, R. D. Schaller, T. Rajh, E. A. Rozhkova, (2013) High-performance bioassisted nano photocatalyst for hydrogen production, ***Nano Letters,*** **13:** 3365-3371.
11. S. Hoang, S. W. Guo, N. T. Hahn, A. J. Bard, C. B. Mullins, (2012) Visible light driven photoelectrochemical water oxidation on nitrogen-modified TiO_2 nanowires, ***Nano Letters***, **12:** 26-32.
12. Y. J. Wang, J. Lin, R. L. Zong, J. He, Y. F. Zhu, (2011) Enhanced photoelectric catalytic degradation of methylene blue via TiO_2 nanotube arrays hybridized with graphite-like carbon, ***Journal of Molecular Catalysis A: Chemical,*** **349:** 13-19.
13. X. Y. Zhan, Q. S. Wang, F. M. Wang, Y. J. Wang, Z. X. Wang, J. L. Cao, M. Safdar, J. He, (2014) Composition-tuned ZnO/ZnxCd1-xTe core/shell nano wires array with broadspectral absorption from UV to NIR for hydrogen generation, ***ACS Applied Materials and Interfaces,*** **6:** 2878-2883.
14. A. Kargar, K. Sun, Y. Jing, C. Choi, H. Jeong, G. Y. Jung, S. Jin, D. L. Wang, (2013) 3D Branched nano wire photoelectrochemical electrodes for efficient solar water splitting, ***ACS Nano,*** **7:** 9407-9415.
15. A. Sheikh, A. Yengantiwar, M. Deo, S. Kelkar, S. Ogale, (2013) Near-field plasmonic functionalization of light harvesting oxide-oxide hetero junctions for efficient solar photo electrochemical water splitting: The AuNP/$ZnFe_2O_4$/ZnO System, ***Small***, **9(12):** 2091-2096.
16. Z. F. Wang, P. Xiao, L. Qiao, X. Q. Meng, Y. H. Zhang, X. L. Li, F. Yang, (2013) Poly pyrrole sensitized ZnO nano rod arrays for efficient photo-electrochemical splitting of water, ***Physica B: Condensed Matter,*** **419:** 51-56.
17. Q. Li, B. D. Guo, J. G. Yu, J. R. Ran, B. H. Zhang, H. J. Yan, J. R. Gong, (2011) Highly efficient visible-light-driven photocatalytic hydrogen production of CdS-cluster-decorated graphene nanosheets, ***Journal of the American Chemical Society,*** **133:** 10878-10884.

18. Jin, J. G. Yu, G. Liu, P. K. Wong, (2013) Singlecrystal CdS nanowires with high visible light photocatalytic H2-production performance, ***Journal of Materials Chemistry A*, 1:** 110927-10934.
19. F. M. Wang, Y. J. Wang, X. Y. Zhan, M. Safdar, J. R. Gong, J. He, (2014) Pt nanoparticle and CdS quantum dot assisted WO_3 nanowires grown on flexible carbon fibers for efficient oxygen production, ***CrystEngComm*, 16:** 1389-1394.
20. P. M. Rao, L. L. Cai, C. Liu, I. S. Cho, C. H. Lee, J. M. Weisse, P. D. Yang, X. L. Zheng, (2014) Simultaneously efficient light absorption and charge separation in $WO_3/BiVO_4$ core/shell nanowire photoanode for photoelectrochemical water oxidation, ***Nano Letters*, 14:** 1099-1105.
21. M. Bagheri, A. R. Mahjoub, A. A. Khodadadi, Y. Mortazavi, (2014) Fast photocatalytic degradation of congo red using CoO-doped β-Ga_2O_3 nanostructures, ***RSC Advances*, 4:** 33262.
22. M. Y. Masoomi A. Morsali, (2013) Morphological study and potential applications of nano metal- organic, ***RSC Advances*, 3:** 19191-19218.
23. M. Y. Masoomi, A. Morsali, (2012) Applications of metal organic coordination polymers as precursors for preparation of nano-materials, ***Coordination Chemistry Reviews*, 256:** 2921-2943.
24. L. B. Liao, Q. H. Zhang, Z. H. Su, Z. Z. Zhao, Y. N. Wang, Y. Li, X. X. Lu, D. G. Wei, G. Y. Feng, Q. K. Yu, X. J. Cai, J. M. Zhao, Z. F. Ren, H. Fang, F. Robles-Hernandez, S. Baldelli, J. M. Bao, (2014) Efficient solar water-splitting using a nanocrystalline CoO photocatalyst, ***Nature Nanotechnology*, 9:** 69-73.
25. H. R. Pouretedal, M. Kiyani, (2014) Photodegradation of 2-nitrophenol catalyzed by CoO, CoS and CoO/CoS nanoparticles, ***Journal of the Iranian Chemical Society*, 11:** 271-277.
26. (a) V. Skumryev, S. Stoyanov, Y. Zhang, G. Hadjipanayis, D. Givord, J. Nogués, (2003) Beating the superparamagnetic limit with exchange bias, ***Nature***, 423: 850. (b) H. K. Lin, H. C. Chiu, H. C. Tsai, S. H. Chien, C. B. Wang, (2003) Synthesis, characterization and catalytic oxidation of carbon monoxide over cobalt oxide, ***Catalysis Letters*, 88:** 169. (c) K. Nakaoka, M. Nakayama, K. Ogura, (2002) Electrochemical deposition of spinel-type cobalt oxide from alkaline solution of Co^{2+} with glycine, ***Journal of the Electrochemical Society*, 149:** C159. (d) M. Ando, T. Kobayashi, S. Iijima, M. Haruta, (1997) Optical recognition of CO and H_2 by use of gas-sensitive Au-Co_3O_4 composite films, ***Journal of Materials Chemistry*, 7:** 1779. (e) N. Koshizaki, K. Yasumoto, T. Sasaki, (2000) Mechanism of optical transmittance change by NOx in CoO/SiO_2 nanocomposites films, ***Sensors and Actuators B: Chemical*, 66:** 122.
27. A. S. Risbud, L. P. Snedeker, M. M. Elcombe, A. K. Cheetham, R. Seshadri, (2005) Wurtzite-to-rocksalt structural transformation in nanocrystalline CoO, ***Chemistry of Materials*, 17:** 834.
28. (a) J. S. Yin, Z. L. Wang, (1997) Ordered self-assembling of tetrahedral oxide nanocrystals, ***Physical Review Letters***, 79: 2570. (b) M. Ghosh, E. V. Sampathkumaran, C. N. R. Rao, (2005) Synthesis and magnetic properties of CoO nanoparticles, ***Chemistry of Materials***, **17:** 2348. (c) N. R. Jana, Y. Chen, X. Peng, (2004) Size and shape-controlled magnetic (Cr, Mn, Fe, Co, Ni) oxide nanocrystals via a simple and general approach, ***Chemistry of Materials*, 16:** 3931.
29. (a) C. Xu, Y. Liu, G. Xu, G. Wang, (2002) Fabrication of CoO nanorods via thermal decompositionof CoC2O4 precursor, ***Chemical Physics Letters*, 366:** 567. (b) W. S. Seo, J. H. Shim, S. J. Oh, E. K. Lee, N. H. Hur, J. T. Park, (2005) Phase-and size-controlled synthesis of hexagonal and cubic CoO nanocrystals, ***Journal of the American Chemical Society*, 127:** 6188. (c) K. An, N. Lee, J. Park, S. C. Kim, Y. Hwang, J. G. Park, J. Y. Kim, J. H. Park, M. J. Han, J. Yu, T. Hyeon. Synthesis, characterization, and self-assembly of pencil-shaped CoOnanorods, ***Journal of the American Chemical Society*, 128:** 9753. (d) J. Park, K. An, Y. Hwang, J. G. Park, H. J. Noh, J. Y. Kim, J. H. Park, N. M. Hwang, T. Hyeon, (2004) Ultra-large-scale synthesis of monodisperse nanocrystals, ***Nature Materials*, 3:** 891.
30. J. S. Yin, Z. L. Wang, (1997) *In situ* structural evolution of self-assembled oxide nanocrystals, ***The Journal of Physical Chemistry B*, 101:** 8979.
31. Y. Zhang, X. Zhong, J. Zhu, Y. Feng, X. Song, (2007) Alcoholysis route to monodisperse CoOnanotetrapods with tunable size, ***Nanotechnology*, 19:** 195605.
32. C. W. Tanga, C. B. Wangb, S. H. Chien, (2008) Characterization of cobalt oxides studied by FT-IR, Raman, TPR and TG-MS, ***Thermochimica Acta*, 473:** 68.
33. X. Zhan, Z. Wang, F. Wang, Z. Cheng, K. Xu, Q. Wang, M. Safdar, H. Jun, (2014) Efficient CoO nanowire array photocatalysts for H2 generation, ***Applied Physics Letters*, 105:** 153903.
34. M. Verelst, T. O. Ely, C. Aminens, E. Snoeck, P. Lecante, A. Mosset, M. Respaud, J. M. Broto, B. Chaudret, (1999) Synthesis and characterization of CoO, Co_3O_4, and mixed Co/CoO nanoparticules, ***Chemistry of Materials*, 11:** 2702.
35. U. A. Fischer, R. Carle, D. R. Kammerer, (2011) Identification and quantification of phenolic compounds from pomegranate (*Punica granatum* L.) peel, mesocarp, aril and differently produced juices by HPLC-DAD–ESI/MS n, ***Food Chemistry*, 127:** 807-821.
36. P. K. Jain, K. S. Lee, I. H. El-Sayed, M. A. El-Sayed, (2006) Calculated absorption and scattering properties of gold nanoparticles of different size, shape, and composition: Applications in biological imaging and biomedicine, ***The Journal of Physical Chemistry B*, 110:** 7238-7248.
37. J. Tauc, (1974) ***Optical Properties of Amorphous Semiconductors" Amorphous and Liquid Semiconductor,*** New York: Plenum, p159.
38. J. G. W. Pratt, R. Coelho, (1959) Optical absorption of CoO and MnO above and below the Neel temperature, ***Physical Review*, 116:** 281.
39. T. D. Thangadurai, N. J. Singh, I. C. Hwang, J. W. Lee, R. P. Chandran, K. S. Kim, (2007) 2-Dimensional analytic approach for anion differentiation with chromofluorogenic receptors, ***The Journal of Organic Chemistry*, 72(14):** 5461-5464.
40. A. V. Ravindra, B. C. Behera, P. Padhan, O. I. Lebedev, W. Prellier, (2014) Tailoring of crystal phase and Neel temperature of cobalt monoxides nanocrystals with synthetic approach conditions, ***Journal of Applied Physics*, 116:** 033912.